A study of the vibronic structure in the HeI excited photoelectron spectrum of CO2 involving the X2g and A2u ionic states

P. Baltzer, F. T. Chau, J. H. D. Eland, L. Karlsson, M. Lundqvist et al.

Citation: J. Chem. Phys. **104**, 8922 (1996); doi: 10.1063/1.471626
View online: http://dx.doi.org/10.1063/1.471626
View Table of Contents: http://jcp.aip.org/resource/1/JCPSA6/v104/i22
Published by the American Institute of Physics.

A study of the vibronic structure in the HeI excited photoelectron spectrum of CO_2 involving the $X\ ^2\Pi_g$ and $A\ ^2\Pi_u$ ionic states

P. Baltzer
Uppsala University, Department of Physics, Box 530, S-751 21 Uppsala, Sweden

F. T. Chau
The Hong Kong Polytechnic University, Department of Applied Biology and Chemical Technology, Hung Hom, Kowloon, Hong Kong

J. H. D. Eland
Physical Chemistry Laboratory, South Parks Road, Oxford OX1 3QZ, United Kingdom

L. Karlsson and M. Lundqvist
Uppsala University, Department of Physics, Box 530, S-751 21 Uppsala, Sweden

J. Rostas
Laboratoire de Photophysique Moléculaire du C.N.R.S. Université de Paris Sud, Batiment 213-91405 Orsay, France

K. Y. Tam
Physical Chemistry Laboratory, South Parks Road, Oxford, OX1 3QZ, United Kingdom

H. Veenhuizen
Institute of Technology, Box 905, S-391 29 Kalmar, Sweden

B. Wannberg
Uppsala University, Department of Physics, Box 530, S-751 21 Uppsala, Sweden

(Received 5 December 1995; accepted 22 February 1996)

The HeI excited photoelectron spectrum of the CO_2 molecule covering the $X\ ^2\Pi_g$ and $A\ ^2\Pi_u$ ionic states has been recorded at a resolution of better than 5 meV. Complex vibrational structures are resolved in both photoelectron bands. In the $X\ ^2\Pi_g$ state, the ν_2 and ν_3 modes are observed to be excited in both an odd and even numbers of quanta in addition to the ν_1 mode, whereas for the $A\ ^2\Pi_u$ state the spectrum is dominated by excitations of the ν_1 mode alone and in combinations with excitations of the ν_2 mode in two quanta involving strong Fermi resonance. The observed spectrum has been assigned by comparison with optical spectra and with calculations of the vibrational fine structure including vibronic and spin–orbit coupling. © *1996 American Institute of Physics.* [S0021-9606(96)01820-X]

I. INTRODUCTION

The first outer valence UV photoelectron spectra of the CO_2 molecule were presented already in the 1960s and 1970s.[1–6] They were well resolved, and showed extensive vibrational structures that provided much information about the properties of the cationic states. Later studies performed with better resolution have further revealed the rich fine structures related to both spin–orbit, Renner–Teller and Herzberg–Teller interactions as well as Fermi resonances.[7–10] Additional information regarding these structures has been obtained by studying the effects of isotopic substitution in the photoelectron spectrum of $^{13}CO_2$.[11] In a more recent study using a supersonic jet target,[12] the rotational and Doppler broadenings were eliminated as well as lines appearing due to inelastic scattering, which gave an even better characterization of the spectrum. In this work also an extensive reference list of spectroscopic works on CO_2 as well as COS and CS_2 up to 1988 can be found.

Threshold photoelectron spectroscopy (TPES) has been carried out at a resolution of about 14 (Ref. 13) and 9 meV (Ref. 14) which has enabled a rather detailed analysis of both the X and A states. The threshold photoelectron spectra may acquire intensity from autoionization processes in addition to direct photoionization and therefore often show vibrational structure that is not observed in conventional photoelectron spectra. This seems to be the case for CO_2^+, where a large number of additional states could be observed particularly in the work of Ref. 14. Excitations of the bending ν_2 mode in single quanta were found to be quite strong, possibly reflecting a bent geometry of the intermediate autoionizing state, which would allow excitations of this mode in odd quanta in the ionic states. Also, high resolution photoionization resonance spectroscopy has been employed in studies of this molecule and from these spectra both the spin–orbit coupling constant and the Renner coupling parameter[15] have been estimated.

Much of the energy level structure has been revealed from studies of infrared and optical spectra of the $A-X$ and $B-X$ band systems (e.g. Refs. 16–27). More recently, the zero-kinetic-energy (ZEKE) photoelectron spectrum was recorded for the $X\ ^2\Pi_g$ state at a resolution of 1.5 cm^{-1}, allowing observation of the rotational fine structure.[28] A review of the literature and an extensive investigation of the

vibronic interactions in the valence states of CO_2^+, in particular with regard to the ν_3 mode, has been presented recently by Johnson and Rostas.[29] These studies have also provided important experimental information for comparison with various theoretically derived quantities.

The present HeI excited spectra show the complex fine structure in greater detail than in previous studies based on electron spectroscopy (except the ZEKE investigation[28]). In particular, we resolve some of the structure related to the excitation of the bending (ν_2) and antisymmetric stretching (ν_3) vibrational modes. By a peak fitting analysis, it has been possible to decompose many of the superimposed lines into their constituents.

II. EXPERIMENTAL DETAILS

The measurements were performed by means of a high resolution UV photoelectron spectrometer that has been described previously.[30] It uses an electrostatic hemispherical analyzer with a mean radius of 144 mm and a microchannel plate detector system. The photoelectrons are focused onto the entrance slit of the analyzer using an electrostatic electron lens. Most of the studies were performed using a gas cell equipped with electrodes for compensation of potential variations due to plasma potentials and varying contact potentials. The most highly resolved spectra were recorded using an effusive molecular beam target, by which the Doppler broadening could be reduced to below 1 meV. All studies were carried out at a resolution better than 5 meV and the linewidth in the spectra recorded from the beam target was about 3 meV. The spectrometer is also designed to give a high signal-to-background ratio, of the order of 10^5. Target gas pressures of a few mtorr were used in the present investigation and at such low pressures lines due to inelastic scattering of photoelectrons, which have been observed in earlier studies,[9] are completely eliminated.

The HeIα radiation that has been employed for the photoionization was produced in a VUV source based on a microwave ECR discharge.[31] The discharge takes place at a pressure of about 50 mtorr in a very small volume between the poles of a strong magnet, which provides a field acting as a magnetic bottle that fulfills the conditions for electron cyclotron resonance in its center. This source gives a very high intensity that facilitates detailed studies. Furthermore, the linewidth of the radiation is very small ($\approx$1 meV).

The sample gas was obtained commercially with a purity of better than 99.99%.

The calibration of the spectra was carried out using the Xe $5p$ lines at 12.130 02 and 13.436 49 eV as energy references.[32] The resulting accuracy in the determination of binding energies for well-defined lines is better than $\pm$0.5 meV. For blended lines the accuracy is of the order of $\pm$1 meV or better.

All spectra are presented as they were obtained originally from the spectrometer, i.e., no deconvolution or background subtraction has been made. In order to determine the energies, widths (FWHM) and relative intensities of the individual vibrational components, a curve fitting program was used where each assumed component was represented by a Gaussian function. The fit was made independently of the optical data and with a minimum number of components. For the A state, Gaussians are not fully satisfactory, since the asymmetry of the line profile caused by the rotational structure is neglected.

III. METHOD USED FOR THE CALCULATION OF RENNER–TELLER COMPONENTS

In the $^2\Pi$ electronic states of the linear CO_2^+ ion, vibronic interaction leads to a breakdown of the Born–Oppenheimer approximation and a complicated energy level pattern for the bending vibrational mode. In the present work, a one-electron model with the inclusion of both vibronic and spin–orbit coupling[33–35] has been adopted to calculate the vibrational energies and, in particular, the intensity distributions of the first and second photoelectron bands of CO_2. The model incorporates a Hamiltonian which considers interaction up to the second order.

Eigenfunctions of the two-dimensional harmonic oscillator were employed for the calculation. Perturbation matrix elements were computed according to formulas given in Ref. 34. The matrix was diagonalized to give vibrational energies. The accuracy of the results was scrutinized by increasing the number of basis functions involved. In addition, the sequential quadratic programming method[36] was used to optimize the dimensionless Renner parameter ϵ, the spin–orbit coupling constant and the vibrational frequency ν_2 to fit the theoretical energies to the experimental values. For symmetry reasons, coupling is possible between different basis functions which have the same total rotational quantum number $K(=\Lambda+l)$ where Λ and l are the electronic and vibrational angular momentum quantum numbers, respectively.

The wave function of the perturbed state of the bending mode is a linear combination of two-dimensional harmonic oscillator functions according to the above coupling treatment. Hence, the transition probability for the ionization process $(0,v_2'',0)\rightarrow(0,v_2',0)$, where v is the vibrational quantum number, is proportional to the square of the sum of vibrational overlap integrals weighted by the corresponding coefficients. The recurrence formulas proposed by Bell and Warsop[37] were used to evaluate the overlap integrals between the two-dimensional harmonic oscillator wavefunctions. From the optimized results, as described above for the vibronic states of the bending mode, theoretical vibrational intensities accompanying the corresponding ionization process can be deduced. For the $(0,v_2'',0)\rightarrow(v_1',v_2',0)$ transition, the intensity was calculated as the product of the observed $(0,0,0)\rightarrow(v_1',0,0)$ intensity and the theoretical $(0,v_2'',0)\rightarrow(0,v_2'',0)$ Franck–Condon factor.

IV. RESULTS AND DISCUSSION

A. The $X\ ^2\Pi_g$ state

Figure 1 shows an overall recording of the photoelectron band at a resolution of about 4–5 meV. The spectrum is dominated by the transitions to the spin–orbit split vibration-

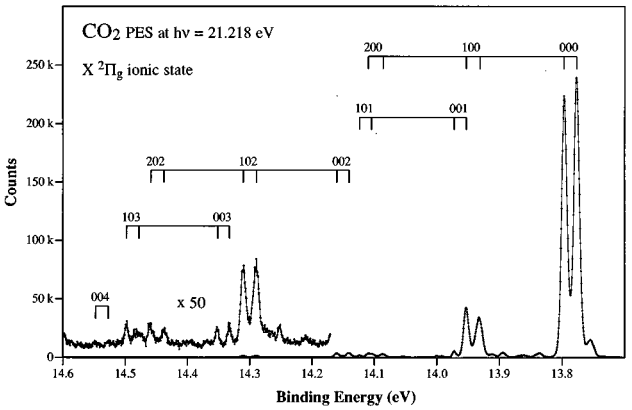

FIG. 1. A HeI-excited spectrum of CO_2 showing the $X\ ^2\Pi_g$ ionic state. Vibrational assignments are given for the nondegenerate modes.

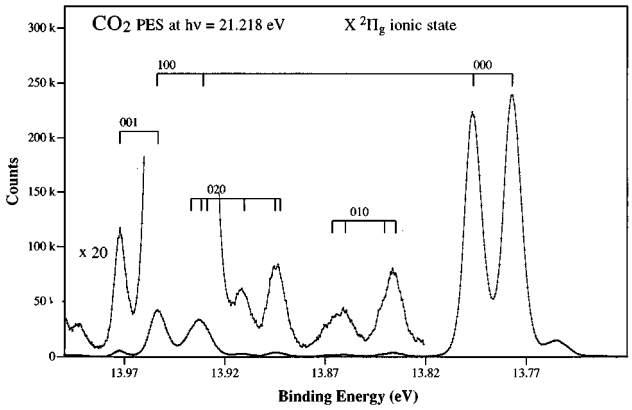

FIG. 2. A high resolution HeI-excited spectrum showing the low energy part of $X\ ^2\Pi_g$ state. The vibrational assignments include all normal modes.

less states, (0,0,0) $^2\Pi_{g,3/2}$ and (0,0,0) $^2\Pi_{g,1/2}$ at 13.7772 and 13.7969 eV, respectively, whereas the vibrational excitations are weak. This agrees well with the fact that the ionization takes place from a very weakly antibonding orbital. Assignments of the most prominent lines are given in this figure in terms of the two stretching modes. They mainly agree with previous studies but involve more energy levels. The antisymmetric ν_3 mode is excited in an even number of quanta but also single and threefold excitations are observed. Weak excitations of the Renner active ν_2 mode are observed in the regions between the more intense features as discussed extensively in previous studies. They will be further discussed in the following.

For the low energy part, the detailed analysis of the line structure has been based upon spectra recorded at a resolution of 3 meV, as shown in Fig. 2, whereas for the parts with very low intensity above 14.2 eV the resolution used was about 4–5 meV. The analysis has been based upon a comparison with other recent studies by Larcher *et al.*,[19] Brommer *et al.*,[26] Chambaud *et al.*,[27] Johnson and Rostas[29] as well as the present calculations. Table I summarizes the result of these studies and includes relevant results of some of the previous work.

Energies and relative intensities have been calculated for some of the observed lines using the model described in Sec. III. The results of these calculations are given in Table II along with relevant experimental data. It can be seen that the energy separations calculated in the present work for various $(0v_20)$ vibronic components mostly agree well (within 2%) with the observed values and that there is at least reasonable agreement with the observed intensities.

The spin–orbit splitting obtained from the positions of the main lines is 19.6 meV, which is 0.2–0.3 meV lower than the values obtained in rotationally resolved studies.[18,23,28] Perfect agreement would probably require resolution of at least the rotational $\Delta N=N^+-N=0$ branch. The two lines are found to have nearly the same intensity, both experimentally and by calculation (cf. Table I). On the low binding energy side of the (000) $^2\Pi_{g,3/2}$ component, a number of hot bands can be seen. Owing to the distribution of energies, the intensities of these fall into three different groups. They are accounted for by our calculations as the (010)–(010), (020)–(020) and, possibly, (030)–(030) transitions (cf. Table II); the agreement with optical data is not perfect but we have not found any other convincing explanation. The low binding energy component of the (010)–(010) transition is clearly observed in Fig. 1, whilst the high energy component is located at approximately the same position as the (000) $^2\Pi_{g,3/2}$ main line and is responsible for the main part of the apparent increase in intensity of this line.

In the region between 13.82 and 13.88 eV, the structure is primarily associated with transitions to the (010) state manifold of the cation. Relative intensities of the various components given in Table I have been deduced by curve fitting. As indicated by the present calculations, some of the intensity in the high energy part of the line centered at 13.866 eV, which is primarily associated with the (010) $^2\Sigma^-$ ionic state, may be caused by (030)–(010) hot band transitions.

At somewhat higher energies, between 13.88 and 13.98 eV, the spectrum involves transitions to both the (020), (100), and (001) ionic states. The transitions to the (020) $\mu\ ^2\Pi_{1/2,3/2}$ states are reflected by the line observed slightly above 13.89 eV. The line exhibits a doublet structure that fits very well with the predicted splitting between the states (cf. Table I). The weak feature at 13.91 eV is mainly a hot band arising from the (110) $\mu\ ^2\Sigma^+$–(010) and (110) $^2\Delta_{5/2}$–(010) transitions that is well predicted by the present calculations (cf. Table II). The (020) $^2\Phi_{7/2}$ state appearing at the same energy is too weak to give an observable intensity.

The two comparatively strong lines in the 13.92–13.96 eV range are primarily associated with the excitation of a single quantum of the ν_1 mode. However, the (020) $\kappa\ ^2\Pi_{1/2,3/2}$ states have nearly the same energy as the (100) $^2\Pi_{3/2}$ state, leading to a strong Fermi resonance between the $\Omega=3/2$ components. As can be seen, the corresponding line is substantially broadened compared to the (100) $^2\Pi_{1/2}$ component and, moreover, the peak maximum is lower, suggesting that the intensity is distributed into both the ionic states. This is confirmed by fitting two Gaussians located at the energies obtained by optical spectroscopy,[26,27] each having the width commonly observed for single lines in this spec-

TABLE I. Experimental energies, relative intensities and assignments of the lines of the $X\ ^2\Pi_g$ state of CO_2^+.

Energy[a] PES (eV)	ΔE[b] PES (meV)	ΔE[b] PES (cm^{-1})	ΔE[b,c,d] optical data (cm^{-1})	PES relative intensity	Assignment
13.713	−64	−516	⋯	0.1	(030)–(030)?
13.733	−44	−355	−335.7	0.5	$(020)\mu\ ^2\Pi_{3/2}$–$(020)^1\Sigma^+$
			−345.6		$(020)\mu\ ^2\Pi_{1/2}$–$(020)^1\Sigma^+$
13.755	−22	−177	−200.2	9.7	$(010)\mu\ ^2\Sigma^+$–$(010)^1\Pi$
			−155.0		$(010)^2\Delta_{5/2}$–$(010)^1\Pi$
13.775	−2	−16	⋯	9.7	$(020)\kappa\ ^2\Pi_{3/2}$–$(020)^1\Sigma^+$
13.7772	0		0	100	$(000)^2\Pi_{3/2}$–$(000)^1\Sigma^+$
13.7969	19.7	159	159.3	100	$(000)^2\Pi_{1/2}$–$(000)^1\Sigma^+$
13.835	58	468	467.2	1.3	$(010)\mu\ ^2\Sigma^+$–$(000)^1\Sigma^+$
13.840*	63	508	512.4	1.0	$(010)^2\Delta_{5/2}$–$(000)^1\Sigma^+$
13.860	83	669	667.8	0.8	$(010)^2\Delta_{3/2}$–$(000)^1\Sigma^+$
13.866*	89	718	719.2	0.8	$(010)\kappa\ ^2\Sigma^-$–$(000)^1\Sigma^+$
13.892*	115	928	939.8	2.3	$(020)\mu\ ^2\Pi_{3/2}$–$(000)^1\Sigma^+$
13.896*	119	960	949.7	0.8	$(020)\mu\ ^2\Pi_{1/2}$–$(000)^1\Sigma^+$
13.911	134	1081	1071.3	1.6	$(110)\mu\ ^2\Sigma^+$–$(010)^1\Pi$
			1089.6		$(110)^2\Delta_{5/2}$–$(010)^1\Pi$
13.931	154	1242	1241.6	11.3	$(100)^2\Pi_{3/2}$–$(000)^1\Sigma^+$
			1281.5		$(110)^2\Delta_{3/2}$–$(010)^1\Pi$
13.937	160	1291	1287.2	7.7	$(020)\kappa\ ^2\Pi_{3/2}$–$(000)^1\Sigma^+$
13.953	176	1420	1423.8	2.2	$(001)^2\Pi_{3/2}$–$(000)^1\Sigma^+$
13.9536	176.7	1425	1426.1	20	$(100)^2\Pi_{1/2}$–$(000)^1\Sigma^+$
13.972	195	1573	1581.7	2.2	$(001)^2\Pi_{1/2}$–$(000)^1\Sigma^+$
13.993	216	1742	1738.7	0.5	$(110)\mu\ ^2\Sigma^+$–$(000)^1\Sigma^+$
14.000	223	1799	1757.0		$(110)^2\Delta_{5/2}$–$(000)^1\Sigma^+$
14.019*	242	1952	1948.9		$(110)^2\Delta_{3/2}$–$(000)^1\Sigma^+$
14.025*	248	2000	1998.4	0.2	$(110)\kappa\ ^2\Sigma^-$–$(000)^1\Sigma^+$
14.052	275	2218	(2218)	0.6	$(120)\mu\ ^2\Pi_{3/2}$–$(000)^1\Sigma^+$
14.055	278	2242	(2236)		$(120)\mu\ ^2\Pi_{1/2}$–$(000)^1\Sigma^+$
14.068	291	2347	2333.1		$(210)\mu\ ^2\Sigma^+$–$(010)^1\Pi$
			(2350)		$(210)^2\Delta_{5/2}$–$(010)^1\Pi$
14.086	309	2492	2496.9	1.5	$(200)^2\Pi_{3/2}$–$(000)^1\Sigma^+$
14.105*	328	2646	(2643)	1.0	[e]$(101)^2\Pi_{3/2}$–$(000)^1\Sigma^+$
14.109	332	2678	2682.4	1.3	$(200)^2\Pi_{1/2}$–$(000)^1\Sigma^+$
		(2685)			[e]$(021)\kappa\ ^2\Pi_{3/2}$–$(000)^1\Sigma^+$
14.124	347	2799	(2819)	1.0	$(101)^2\Pi_{1/2}$–$(000)^1\Sigma^+$
14.1408	363.6	2933	2938.4	1.9	$(002)^2\Pi_{3/2}$–$(000)^1\Sigma^+$
14.1605	383.3	3092	3095.3	1.9	$(002)^2\Pi_{1/2}$–$(000)^1\Sigma^+$
14.209	432	3484	(3483)	0.1	$(220)\mu\ ^2\Pi_{3/2}$–$(000)^1\Sigma^+$
14.252	475	3831	3820.5	0.1	$(220)\mu\ ^2\Pi_{1/2}$–$(000)^1\Sigma^+$
14.289	512	4130	4127.8	0.6	$(102)^2\Pi_{3/2}$–$(000)^1\Sigma^+$
14.310	533	4299	4306.5	0.6	$(102)^2\Pi_{1/2}$–$(000)^1\Sigma^+$
14.332	555	4476	(4545)	0.1	$(003)^2\Pi_{3/2}$–$(000)^1\Sigma^+$
14.351	574	4630	(4700)	0.1	$(003)^2\Pi_{1/2}$–$(000)^1\Sigma^+$
14.438	661	5331	5331.9	0.1	$(202)^2\Pi_{3/2}$–$(000)^1\Sigma^+$
14.459	682	5501	5512.6	0.1	$(202)^2\Pi_{1/2}$–$(000)^1\Sigma^+$
14.478	701	5654	(5713)	0.1	$(103)^2\Pi_{3/2}$–$(000)^1\Sigma^+$
14.498	721	5815	(5885)	0.1	$(103)^2\Pi_{1/2}$–$(000)^1\Sigma^+$
14.527	750	6049	⋯	0.05	$(004)^2\Pi_{3/2}$–$(000)^1\Sigma^+$
14.547	770	6210	⋯	0.05	$(004)^2\Pi_{1/2}$–$(000)^1\Sigma^+$

[a]Unresolved components are marked with an asterisk (*).

[b]$\Delta E = [E(CO_2^+, X, v_1v_2v_3) - E(CO_2, X, v_1v_2v_3)] - [E(CO_2^+, X\ ^2\Pi_{3/2,g}, 000) - E(CO_2, X\ ^1\Sigma_g^+, 000)]$.

[c]Parenthetical figures are *ab initio* values of Ref. 26.

[d]Italic figures are values calculated using a model, including RT, Fermi, S–O interactions and anharmonicities (x_{ij}), with the parameters determined from the fit of about 50 vibronic levels. For most of the observed levels, |obs–calc|<5 cm^{-1}. Since the *ab initio* potential curve (Ref. 26) has been corrected in order to fit the observed levels, the calculated values for the levels with $v_3=3$ are probably fairly inaccurate, because the anharmonicity parameters involving v_3 are poorly determined.

[e]These two states are totally mixed through Fermi interaction.

TABLE II. Energies and relative intensities calculated for some lines of the $X\ ^2\Pi_g$ state using the model described in Sec. III.

Energy PES (eV)	Spacing PES (meV)	Relative intensity PES	Calculated energy[a] (meV)	Calculated intensity[b]	Assignment
13.713	−64	0.1	−52.3	0.12	(030)–(030)?
13.733	−44	0.5	−47.1	0.10	$(020)\mu\ ^2\Pi_{1/2}$–$(020)^1\Sigma^+$
13.755	−22	9.7	−24.8	6.11	$(010)\mu\ ^2\Sigma^+$–$(010)^1\Pi$
13.7772	0	100	0.0	100[c]	$(000)^2\Pi_{3/2}$–$(000)^1\Sigma^+$
13.7969	19.7	100	19.0	99.7	$(000)^2\Pi_{1/2}$–$(000)^1\Sigma^+$
13.892	115	2.3	117.4	1.60	$(020)\mu\ ^2\Pi_{3/2}$–$(000)^1\Sigma^+$
13.896	119	0.8	118.4	2.46	$(020)\mu\ ^2\Pi_{1/2}$–$(000)^1\Sigma^+$
13.911	134	1.6	132.9	0.86	$(110)\mu\ ^2\Sigma^+$–$(010)^1\Pi$
			135.2	0.54	$(110)^2\Delta_{5/2}$–$(010)^1\Pi$
			159.0[d]	0.53[e]	$(110)^2\Delta_{3/2}$–$(010)^1\Pi$
13.937	160	7.7	162.1	1.21	$(020)\kappa\ ^2\Pi_{3/2}$–$(000)^1\Sigma^+$

[a]Calculations based on a one-electron model (see text) with $\epsilon=-0.213$, $A=-19.2$ meV, $\nu_2''=82.730$ meV, and $\nu_2'=65.306$ meV.

[b]Intensity calculation based on a two-dimensional harmonic oscillator with $\nu_2''=82.730$ meV and $\nu_2'=65.306$ meV.

[c]The intensity was normalized to 100 for the strongest line.

[d]The calculated energy was obtained by subtracting ν'' from the observed energies for (110) vibronic components (Ref. 27).

[e]The intensity is calculated as the product of the observed intensities of the two (100) components and the calculated intensity of the (010)–(010) transition.

trum. A very good representation of the observed line is obtained using the peak heights given in Table I. As can be seen, the peak corresponding to the (020) $\kappa\ ^2\Pi_{3/2}$ state is more than three times as intense as the (020) $\mu\ ^2\Pi_{3/2}$ peak which gives a clear indication that the mixing between the (100) $^2\Pi_{3/2}$ and (020) $\kappa\ ^2\Pi_{3/2}$ states is very significant. The calculation predicts a much smaller intensity difference as expected. The model used does not include Fermi resonances and is therefore incapable of accounting for the high intensity of the mixed components, such as (020) $\kappa\ ^2\Pi_{1/2,3/2}$, while the agreement with the experimental result for the (020) $\mu\ ^2\Pi_{1/2,3/2}$ states and other unmixed states is reasonable. The 100/020 Fermi resonance has been studied in detail[18] and it has been shown that 100 $^2\Pi_{3/2}$ and 020 $\kappa\ ^2\Pi_{3/2}$ are almost totally mixed.

Excitations of the antisymmetric ν_3 mode have been noticed in some previous studies.[10,12,14] In the present spectrum, the (0,0,1) $^2\Pi_{u,1/2}$ component is well resolved at 13.972 eV while the corresponding (0,0,1) $^2\Pi_{u,3/2}$ peak is hidden under the (1,0,0) $^2\Pi_{g,1/2}$ peak (cf. Table I). This excitation can be explained by Herzberg–Teller interaction involving the $A\ ^2\Pi_u$ state as discussed most recently in Ref. 29. Similar excitations are observed also in the photoelectron spectrum of CS_2 where they are even stronger and dominate the vibrational spectrum.[38]

In the 13.98–14.07 energy range, single and double excitations of the ν_2 mode reappear in combination with a quantum of the ν_1 mode. As can be seen from Fig. 3, the line shapes and relative intensities are similar to those observed for the ν_2 mode alone in the 13.82–13.90 eV range. The energies and intensities are summarised in Table I.

The next region showing considerable intensity is that between 14.08 and 14.18 eV. In this range, lines corresponding to both the (200) and (002) ionic states are readily identified at positions that agree very well with the results of other experimental and theoretical studies carried out recently[26,27,29] (cf. Table I). The expanded view in Fig. 3 shows, however, the presence of a weaker line at 14.124 eV in the center of the group. In addition, the second line slightly above 14.10 eV is strongly broadened. This shows that also other states acquire a non-negligible intensity. Energetically, both the (101) and the high energy component of (120) are conceivable. A comparison with the results of Ref. 26 suggests, however, that the line at 14.124 eV should be associated with the (101) $^2\Pi_{1/2}$ state, whereas the (120) $\kappa\ ^2\Pi_{3/2,1/2}$ states are located closer to the (200) $^2\Pi_{1/2,3/2}$ states and most likely gives rise to the intensity between the corresponding lines in the spectrum. The broadening of the line slightly above 14.10 eV is clearly caused by a non-negligible

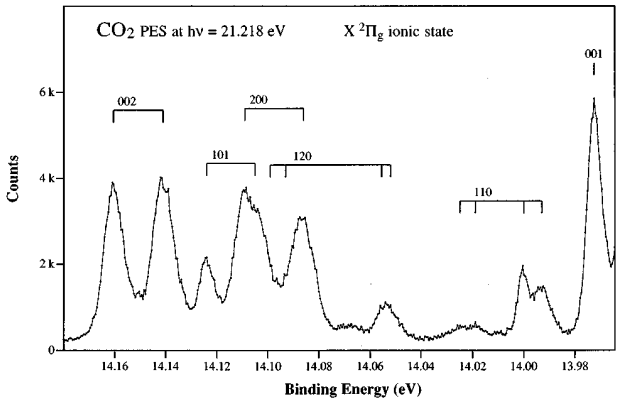

FIG. 3. A detail of the HeI-excited spectrum showing the 13.96–14.17 eV region of the $X\ ^2\Pi_g$ state.

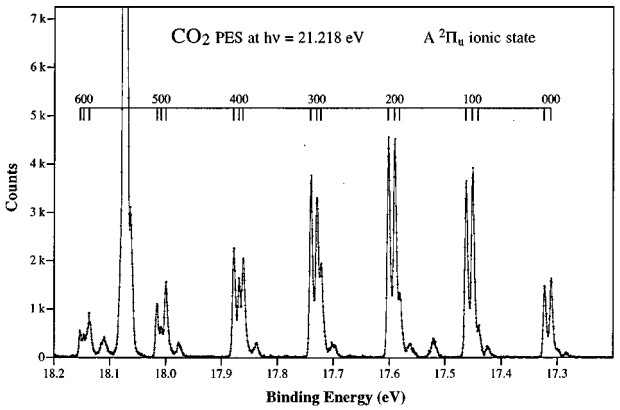

FIG. 4. A high resolution HeI-excited spectrum of CO_2 showing the $A\ ^2\Pi_u$ ionic state. Vibrational assignments involve the ν_1 mode. Due to the Fermi resonance, the $^2\Pi_{3/2}$ $(v_1 00)$ and $^2\Pi_{3/2}$ $(v_1-1,2,0)$ states are strongly mixed and, therefore, three lines are marked in the bar diagram for each $^2\Pi_{1/2,3/2}$ $(v_1 00)$ ionic state. The strong line at 18.0761 eV is due to transitions to the $B\ ^2\Sigma_u^+$ (000) state and the line at 17.55 eV corresponds to the $C\ ^2\Sigma_g^+$ (000) ionic state excited with the HeI β radiation at 23.087 eV.

intensity going into the (101) $^2\Pi_{3/2}$ component. This behavior is expected since the (101) $^2\Pi_{1/2,3/2}$ components have *ungerade* symmetry and therefore acquire their intensities primarily via Herzberg–Teller interaction with the $A\ ^2\Pi_u$ state. They should therefore be expected to have similar intensity, as was obtained in the curve fitting procedure. It may be noted finally, that a 1–1 hot band in the ν_2 mode precedes the first line associated with the (200) $^2\Pi_{g,3/2}$ state as observed for the (100) $^2\Pi_{g,3/2}$ and (000) $^2\Pi_{g,3/2}$ excitations.

Above 14.2 eV the spectrum has very low intensity. However, several lines are well resolved. The most prominent peaks appearing at 14.3 eV must, for both energy and intensity reasons, be associated with the (102) final states, whilst the two weaker features at 14.332 and 14.351 eV can be associated with the (003) states. Since the energy of the ν_3 mode increases slightly with the number of quanta, the components of the (103) excitation are expected to appear slightly below 14.5 eV, where two lines are seen. These lines were earlier associated with the (004) state,[12] but to obtain a consistent assignment, the (004) transitions must rather be ascribed to the pair of very weak lines slightly above 14.5 eV. The remaining two lines in the region between 14.4 and 14.5 eV can for both energy and intensity reasons be assigned to the (202) final states. It may be noted that for the $(v_1 02)$ states with $v_1=0,1,2$, there is a very satisfactory agreement with the recent energies presented by Johnson and Rostas.[29]

The Renner parameter ϵ, the spin–orbit coupling constant A and the vibrational frequency ν_2 fitted to the present experimental data are listed in a footnote of Table II. Earlier values obtained from different spectroscopic techniques are given in Refs. 9, 15, 18, 19, 24, and 25 and from a molecular orbital study in Ref. 26. The present values are close to those obtained previously but should be regarded only as fitting parameters.

B. The $A\ ^2\Pi_u$ state

The spectrum corresponding to this state is dominated by the well-known progression in the ν_1 mode. Each line in this progression is expected to be split by spin–orbit interaction into two components and these have just barely been resolved in previous studies. In addition, earlier studies have revealed a weaker feature on the low binding energy side of the main lines which has been associated with both a hot band and the $(v_1$-1,2,0) progression.[7–12]

An overall recording of the band at a resolution of about 3 meV is shown in Fig. 4 covering the 17.2–18.2 eV energy range. In this spectrum, the line structure appears much more clearly than in previous studies and it is readily seen that each of the main lines consists of three components, rather than two, and that the shape of the structure on the low energy side gradually changes as the energy increases. The observed lines are still partly overlapping and in order to analyze the spectrum in detail, curve fittings have been done to provide energies and relative intensities. The results are collected in Table III together with optical data from other works. The details of the line structure and the assignments are discussed in the following.

As for the X state, energies and relative intensities have been calculated for some of the observed lines using the model described in Sec. III. The results of these calculations are given in Table IV along with relevant experimental data. As can be seen, the discrepancies between the present calculated results for the bending mode and the corresponding experimental data are small (within $\pm 2.5\%$) which supports our interpretation of the spectral features associated with this mode.

The first two peaks of the main progression, corresponding to the $A\ ^2\Pi_u$ (000)$\leftarrow X\ ^1\Sigma_g^+$ (000) transition, are observed at 17.3132 and 17.3250 eV, respectively. The former value is thus the adiabatic binding energy for the A state. The spin–orbit splitting obtained from these energies is 11.8 meV, which is in good agreement with the value of 11.86 meV obtained from optical spectroscopy.[29] These two lines are preceded by resolved weaker features at 17.286 and 17.300 eV, reflecting the(010)–(010) hot band transition as can be seen by comparison to the present calculations (cf. Fig. 5 and Table IV). The apparent intensity of the $^2\Pi_{3/2}$ (000) component is slightly higher than the $^2\Pi_{1/2}$ (000) component. The difference is insignificant from the point of view of our calculations. It is not primarily due to a superposition of a hot band, but seems to be caused by an overlap with the higher energy component which has an asymmetric line shape with a tail on the low binding energy side reflecting the rotational substructure.

The (100)$\leftarrow$(000) line and the accompanying (110)$\leftarrow$(010) hot bands in the 17.4–17.5 eV range show essentially the same relative intensities as the first line manifold, as can be seen from Fig. 5. However, the lowest hot band component at 17.426 eV exhibits a pronounced tail which indicates that additional excitations are present. We suggest that this structure, located at about 17.419 eV, reflects weak (020)$\leftarrow$(000) excitations with an energy of about

TABLE III. Experimental energies, relative intensities and assignments of lines of the $A\ ^2\Pi_u$ state of CO_2^+.

Energy[a] PES (eV)	ΔE[b] PES (meV)	ΔE[b] PES (cm^{-1})	ΔE[b,c] Optical data (cm^{-1})	PES relative intensity	Assignment
17.286	−27	−218	−226.4	2.9	$(010)^2\Delta_{5/2}-(010)^1\Pi$
17.300*	−13	−105	−98.8	2.9	$(010)\kappa\ ^2\Sigma^- - (010)^1\Pi$
17.3132	0	0	0	36.3	$(000)^2\Pi_{3/2}-(000)^1\Sigma^+$
17.3250	11.8	95	95.32	31.9	$(000)^2\Pi_{1/2}-(000)^1\Sigma^+$
17.368	55	444	440.9	0.2	$(010)\mu\ ^2\Sigma^+ - (000)^1\Sigma^+$
17.39	77	621	568.8	0.1	$(010)\kappa\ ^2\Sigma^- - (000)^1\Sigma^+$
17.399	86	694	(648)	0.1	$(030)\mu\ ^2\Sigma^+ - (010)^1\Pi$
17.419*	106	855	(883,886)	1.8	$(020)\mu\ ^2\Pi_{3/2,1/2}-(000)^1\Sigma^+$
17.426	113	911	905.7	5.9	$(110)\mu\ ^2\Sigma^+ - (010)^1\Pi$
17.440*	127	1024	1035.2	5.9	$(110)\kappa\ ^2\Sigma^- - (010)^1\Pi$
17.443*	129	1043	(1037)	11.0	$(020)\kappa\ ^2\Pi_{3/2}-(000)^1\Sigma^+$
17.4529	139.7	1127	1126.9	86.8	$(100)^2\Pi_{3/2}-(000)^1\Sigma^+$
17.4643	151.1	1219	1221.3	79.1	$(100)^2\Pi_{1/2}-(000)^1\Sigma^+$
17.507	194	1565	1573.1	0.2	$(110)\mu\ ^2\Sigma^+ - (000)^1\Sigma^+$
17.559*	246	1984	(1963)	3.3	$(120)\mu\ ^2\Pi_{3/2,1/2}-(000)^1\Sigma^+$
17.565	252	2033	2035.4	8.8	$(210)\mu\ ^2\Sigma^+ - (010)^1\Pi$
17.579*	266	2145	2168.0	8.8	$(210)\kappa\ ^2\Sigma^- - (010)^1\Pi$
17.583	270	2179	(2174)	26.4	$(120)\kappa\ ^2\Pi_{3/2,1/2}-(000)^1\Sigma^+$
17.5920	278.8	2249	2249.5	100.0	$(200)^2\Pi_{3/2}-(000)^1\Sigma^+$
17.6031	289.9	2338	2342.1	100.0	$(200)^2\Pi_{1/2}-(000)^1\Sigma^+$
17.646	333			0.6	$(210)\mu\ ^2\Sigma^+ - (000)^1\Sigma^+$
17.672	359	2896	(2897)	1.0	$(140)\mu\ ^2\Pi_{3/2,1/2}-(000)^1\Sigma^+$
			(2902)		$(230)\mu\ ^2\Sigma^+ - (010)^1\Pi$
17.699*	386	3113	(3109)	3.3	$(220)\mu\ ^2\Pi_{3/2,1/2}-(000)^1\Sigma^+$
			(3116)		$(230)\kappa\ ^2\Sigma^- - (010)^1\Pi$
17.704*	391	3154	(3155)	7.3	$(310)\mu\ ^2\Sigma^+ - (010)^1\Pi$
			(3156)		$(140)\kappa\ ^2\Pi_{3/2,1/2}-(000)^1\Sigma^+$
17.718*	405	3267	(3307)	7.3	$(310)\kappa\ ^2\Sigma^- - (010)^1\Pi$
17.7233	410.1	3308	(3309)	41.8	$(220)\kappa\ ^2\Pi_{3/2,1/2}-(000)^1\Sigma^+$
17.7307	417.5	3367	3369.6	73.6	$(300)^2\Pi_{3/2}-(000)^1\Sigma^+$
17.7414	428.2	3454	3458.7	82.4	$(300)^2\Pi_{1/2}-(000)^1\Sigma^+$
17.784	471	3799	3821.5	0.8	$(310)\mu\ ^2\Sigma^+ - (000)^1\Sigma^+$
17.811	498	4017	(3961)	0.9	$(310)\kappa\ ^2\Sigma^- - (000)^1\Sigma^+$
			(4041)		$(330)\mu\ ^2\Sigma^+ - (010)^1\Pi$
17.8379	524.7	4232	(4247)	5.1	$(330)\kappa\ ^2\Sigma^- - (010)^1\Pi$
			(4246,4253)		$(320)\mu\ ^2\Pi_{3/2,1/2}-(000)^1\Sigma^+$
17.843*	530	4275	(4276)	5.0	$(410)\mu\ ^2\Sigma^+ - (010)^1\Pi$
17.852*	539	4347	(4418)	5.0	$(410)\kappa\ ^2\Sigma^- - (010)^1\Pi$
17.8627	549.5	4432	4432.1	45.1	$(320)\kappa\ ^2\Pi_{3/2}-(000)^1\Sigma^+$
17.8698	556.6	4489	4489.6	36.3	$(400)^2\Pi_{3/2}-(000)^1\Sigma^+$
17.8793	566.1	4566	4570.5	49.5	$(400)^2\Pi_{1/2}-(000)^1\Sigma^+$
17.923	610	4920	(4914)	1.1	$(330)\kappa\ ^2\Sigma^- - (000)^1\Sigma^+$
			(4943)		$(410)\mu\ ^2\Sigma^+ - (000)^1\Sigma^+$
17.949	636	5130	(5170)	1.1	$(430)\mu\ ^2\Sigma^+ - (010)^1\Pi$
17.977*	664	5356	(5366)	5.5	$(430)\kappa\ ^2\Sigma^+ - (010)^1\Pi$
					$(420)\mu\ ^2\Pi_{3/2,1/2}-(000)^1\Sigma^+$
17.982*	669	5396	(5399)	2.9	$(510)\mu\ ^2\Sigma^+ - (010)^1\Pi$
17.996*	683	5509	(5540)	2.9	$(510)\kappa\ ^2\Sigma^- - (010)^1\Pi$
18.0006	687.4	5544	(5544.9)	34.3	$(420)\kappa\ ^2\Pi_{3/2}-(000)^1\Sigma^+$
			(5568)		$(420)\kappa\ ^2\Pi_{1/2}-(000)^1\Sigma^+$
18.0089	695.7	5611	5611.4	14.3	$(500)^2\Pi_{3/2}-(000)^1\Sigma^+$
18.0165	703.3	5673	5679.0	24.2	$(500)^2\Pi_{1/2}-(000)^1\Sigma^+$
18.1105	797.3	6431	6395.1	8.4	$(102)^2\Pi_{3/2}-(000)^1\Sigma^+$
18.116*	802.8	6475	(6477)	5.3	$(530)\kappa\ ^2\Sigma^- - (010)^1\Pi$
					$(520)\mu\ ^2\Pi_{3/2,1/2}-(000)^1\Sigma^+$
			6492.2		$(102)^2\Pi_{1/2}-(000)^1\Sigma^+$
18.120*	807	6509	(6523)	2.3	$(610)\mu\ ^2\Sigma^+ - (010)^1\Pi$
18.134*	821	6622	⋯	2.3	?
18.138	825	6654	6648.8	19.8	$(520)\kappa\ ^2\Pi_{3/2}-(000)^1\Sigma^+$
			(6663)		$(610)\kappa\ ^2\Sigma^- - (010)^1\Pi$
18.1473	834.1	6727	6739	9.9	$(600)^2\Pi_{3/2}-(000)^1\Sigma^+$
18.1540	840.8	6782	6786	11.4	$(600)^2\Pi_{1/2}-(000)^1\Sigma^+$
18.2735	960.3	7745	7746.3	8.4	$(620)\kappa\ ^2\Pi_{3/2}-(000)^1\Sigma^+$
18.290	977	7880	(7868)	3.9	$(700)^2\Pi_{3/2}-(000)^1\Sigma^+$

TABLE III. (*Continued*.)

Energy[a] PES (eV)	ΔE[b] PES (meV)	ΔE[b] PES (cm^{-1})	ΔE[b,c] Optical data (cm^{-1})	PES relative intensity	Assignment
			7907.0		$(700)^2\Pi_{1/2}-(000)^1\Sigma^+$
18.409	1096	8840		3.2	[d]$(720)\kappa\,^2\Pi_{3/2}-(000)^1\Sigma^+$
18.426	1113	8977		1.2	[d]$(800)^2\Pi_{1/2}-(000)^1\Sigma^+$
18.544	1231	9929		1.2	[d]$(820)\kappa\,^2\Pi_{3/2}-(000)^1\Sigma^+$
18.561	1248	10 066		0.3	[d]$(900)^2\Pi_{1/2}-(000)^1\Sigma^+$
18.679	1366	11 017		0.4	[d]$(920)\kappa\,^2\Pi_{3/2}-(000)^1\Sigma^+$

[a]Unresolved components are marked with an asterisk (*).
[b]$\Delta E=[E(CO_2^+, A, v_1v_2v_3)-E(CO_2, X, v_1v_2v_3)]-[E(CO_2^+, A^2\Pi_{3/2,u}, 000)-E(CO_2, X\ ^1\Sigma_g^+, 000)]$.
[c]Parenthetical figures are values calculated using a model, including RT, Fermi, S–O interactions and anharmonicities (x_{ij}), with the parameters determined from the fit of about 45 vibronic levels. For most of the observed levels, $|\text{obs}-\text{calc}|<5\ cm^{-1}$.
[d]These levels have not been calculated.

106 meV. This interpretation is supported by the observations of the higher energy lines.

A detail of the third and fourth groups of lines is shown in Fig. 6. For these, the spin–orbit splitting between the main lines is reduced to 11.2 and 10.7 meV, respectively, and the additional line on the low binding energy side of the $(v_1 00)^2\Pi_{3/2}$ component increases dramatically in intensity between $v_1=2$ and 3. Moreover, the weaker structures further out on the low binding energy side are more pronounced than for the (000) and (100) lines. The obvious interpretation is that the hot bands remain approximately unchanged, relatively, while progressions involving $(v_1-1,2,0)$ excitations become progressively more intense, presumably due to stronger interaction. The $(v_1-1,2,0)$ $\kappa\,^2\Pi_{3/2}$ states are close in energy to the $(v_1,0,0)^2\Pi_{3/2}$ states and may therefore be strongly mixed by Fermi resonance. Thus, the remarkable

TABLE IV. Energies and relative intensities calculated for some lines of the $A\ ^2\Pi_u$ state using the model described in Sec. III.

Binding energy (eV)	Vibr. energy (meV)	Relative intensity PES	Calculated energy[a] (meV)	Calculated intensity[a]	Assignment
			−30.4	2.21	$(010)\mu\,^2\Sigma^+-(010)^1\Pi$
17.286	−27	2.9	−28.8	1.23	$(010)^2\Delta_{5/2}-(010)^1\Pi$
			−14.3	1.19	$(010)^2\Delta_{3/2}-(010)$
17.300	−13	2.9	−12.2	0.26	$(010)\kappa\,^2\Sigma^--(010)^1\Pi$
17.3132	0	36.3	0.0	31.9	$(000)^2\Pi_{3/2}-(000)^1\Sigma^+$
17.3250	11.8	31.9	14.2	36.9[b]	$(000)^2\Pi_{1/2}-(000)^1\Sigma^+$
17.426	113	5.9		4.25[c]	$(110)\mu\,^2\Sigma^+-(010)^1\Pi$
17.440	127	5.9		3.87[c]	$(110)\kappa\,^2\Sigma^--(010)^1\Pi$
			126.3	1.07	$(020)\kappa\,^2\Pi_{1/2}-(000)^1\Sigma^+$
17.4425	129.3	11.0	126.6	1.03	$(020)\kappa\,^2\Pi_{3/2}-(000)^1\Sigma^+$
17.565	252	8.8		4.89[c]	$(210)\mu\,^2\Sigma^+-(010)^1\Pi$
17.579	266	8.8		4.89[c]	$(210)\kappa\,^2\Sigma^--(0,1,0)^1\Pi$
17.5833	270.1	26.4		1.85[d]	$(120)\kappa\,^2\Pi_{3/2,1/2}-(0,0,0)^1\Sigma^+$
17.704	391	7.3		3.60[c]	$(310)\mu\,^2\Sigma^+-(0,1,0)^1\Pi$
17.7233	410.1	41.8		2.10[d]	$(220)\kappa\,^2\Pi_{3/2,1/2}-(000)^1\Sigma^+$
17.843	530	5.0		1.78[c]	$(410)\mu\,^2\Sigma^+-(010)^1\Pi$
17.8627	549.5	45.1		1.63[d]	$(320)\kappa\,^2\Pi_{3/2}-(000)^1\Sigma^+$
17.982	669	2.9		0.70[c]	$(510)\mu\,^2\Sigma^+-(010)^1\Pi$
18.0006	687.4	34.3		0.90[d]	$(420)\kappa\,^2\Pi_{1/2,3/2}-(000)^1\Sigma^+$
18.120	807	2.3		0.48[c]	$(610)\mu^2\Sigma^+-(010)^1\Pi$
18.138	825	19.8		0.41[d]	$(520)\kappa\,^2\Pi_{3/2}-(000)^1\Sigma^+$
18.2735	960.3	8.4		0.22[d]	$(620)\kappa\,^2\Pi_{3/2}-(000)^1\Sigma^+$

[a]Calculations based on a one-electron model (see text) with $\epsilon=-0.100$, $A=-14.8$ meV, $\nu_2''=82.730$ meV and $\nu_2'=55.257$ meV.
[b]The calculated intensities were normalized to the experimental value for this line, where the experimental intensities are normalized to 100 for the strongest line (2,0,0).
[c]The intensity is calculated as the product of the observed intensity of the $(v',0,0)$ component and the calculated intensities of the $(0,v_2'',0)-(0,v_2',0)$ transitions with a given v_2'' level and various vibronic states with the same v_2'.
[d]The intensity is calculated as the product of the average of the observed intensities of the two $(v',0,0)$ components and the calculated intensity of the (0,2,0)–(0,0,0) transition for the corresponding vibronic state.

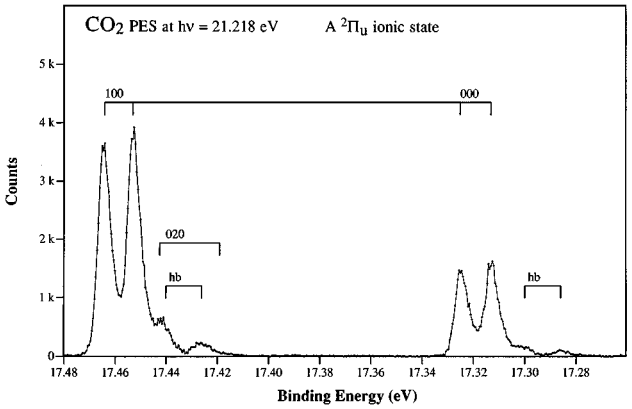

FIG. 5. A detail of the HeI-excited spectrum in the range of the transitions to the (000) and (100) states of $A\ ^2\Pi_u$ state. The bar diagrams in this and later figures identifies the spin-orbit components of the main ν_1 progression.

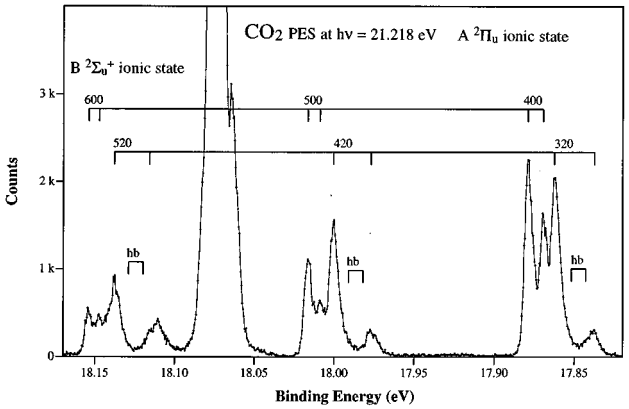

FIG. 7. A detail of the HeI-excited spectrum in the range of the (400), (500), and (600) components of $A\ ^2\Pi_u$ state.

increase in intensity of the $(v_1{-}1,2,0)$ $\kappa\ ^2\Pi_{3/2}$ components would take place at the expense of the intensity of the $(v_1,0,0)$ $^2\Pi_{3/2}$ line, which is in qualitative agreement with the observations. Some intensity may also be transferred from the $(v_1,0,0)$ $^2\Pi_{1/2}$ component to the $(v_1{-}1,2,0)$ $\kappa\ ^2\Pi_{1/2}$ component. It is nevertheless puzzling that the sum of the intensities of the strongly mixed components becomes relatively much greater than that of the unmixed ones. One possible mechanism to explain the observation is a change in Franck–Condon factors in response to anharmonic coupling between the ν_1 and ν_2 modes.

Figure 7 shows the detailed line structure in the range of the (400), (500), and (600) final states. The general structure and the gradual changes are the same as observed for the components at lower energy. Thus, the excitations involving the ν_2 mode are even more pronounced, the intensity of the $(v_1 00)$ $^2\Pi_{3/2}$ line decreases even further and the spin–orbit splitting in the $(v_1 00)$ progression decreases.

From these observations, we conclude that each main group of lines in the spectrum is composed essentially of six lines, two associated with the $(v_1,00)$ $^2\Pi_{1/2,3/2}$ ionic states, two associated with the $(v_1{-}1,2,0)$ $\mu\ ^2\Pi_{1/2,3/2}$ and $(v_1{-}1,2,0)$ $\kappa\ ^2\Pi_{1/2,3/2}$ ionic states (the two spin–orbit split components of each of these are most likely not resolved) and two lines corresponding to the $(v_1,1,0)\leftarrow(0,1,0)$ hot band transitions. The energies and relative intensities of these were deduced by curve fittings as mentioned above. Since the rotational line profile could not be determined, the fittings were made by representing each line with a Gaussian, and are therefore somewhat approximate. It may be noted, however, that the energies deduced in all cases are very close to the energy for the intensity maximum of the experimental line. The hot bands are not resolved in general and their relative positions and widths were therefore taken to be the same as observed on the low binding energy side of the (000) lines.

In the (600)–(520) complex, an additional line appears at 18.1105 eV. This line has been observed previously, although not as well resolved, and has from angle resolved studies been associated with transitions to the (102) ionic state.[10] The other component of the spin–orbit split state is expected to appear at 18.120 eV, but the intensity in this range is low.

At energies above 18.15 eV, the overlap with the vibrational structure of the $B\ ^2\Sigma_u^+$ state is substantial. Nevertheless, it is possible to follow the $(v_1{-}1,2,0)$ $\kappa\ ^2\Pi_{1/2,3/2}$ and

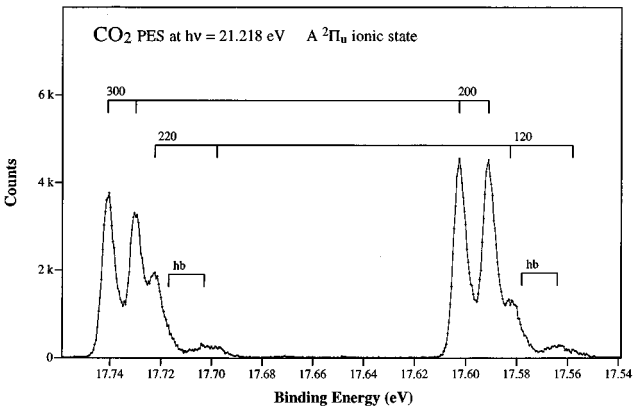

FIG. 6. A detail of the HeI-excited spectrum in the range of the transitions to the (200) and (300) states of $A\ ^2\Pi_u$ state. The additional bar diagrams here and in Fig. 7 indentify the $\mu\ ^2\Pi$ and $\kappa\ ^2\Pi$ members of the Renner–Teller and spin-orbit split multiplets arising from the $(v_1,2,0)$ levels.

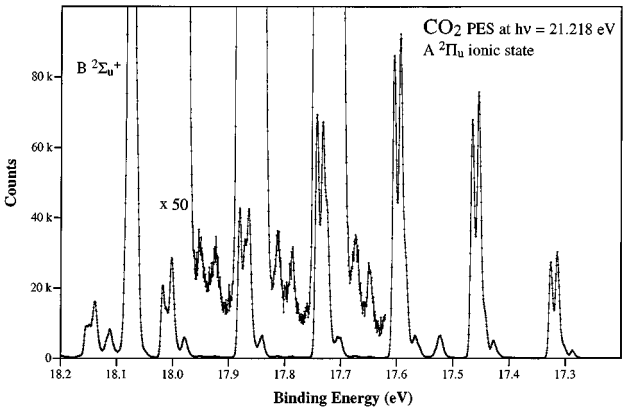

FIG. 8. A recording of the $A\ ^2\Pi_u$ state showing the low intensity lines associated with excitations of ν_2 in single quanta and hot band transitions.

$(v_1,0,0)\ ^2\Pi_{1/2}$ progressions up to the $v_1=9$ components, and to determine the relative intensities. In this energy range, the splitting of the $(v_1,0,0)\ ^2\Pi_{1/2,3/2}$ states becomes very small. However, it seems that the main part of the intensity is acquired by the $\Omega=1/2$ component.

Two additional series of very weak structures are observed in the intervals between the main lines, as can be seen in Fig. 8. The energies and intensities of these features are given in Table III. In earlier studies, structures observed in this region have been associated with excitations of a single quantum of the ν_2 mode. The present theoretical study corroborates this interpretation for the first line, which fits well with the $(v_1 10)\ \mu\ ^2\Sigma^+$ ionic state. Although the second line, which is about 25 meV higher in energy, could have some contributions from the same state manifold, the calculations suggest that it should rather be associated with a hot band corresponding to $(n30)\leftarrow(010)$ transitions.

Finally, by minimizing the discrepancies between the observed and theoretical vibronic energies of $(0v_20)$, the Renner parameter, spin–orbit coupling constant and the ν_2 frequency of the $A\ ^2\Pi_u$ cationic state were determined to be, respectively, $\epsilon=-0.100\pm0.005$, $A=-14.8\pm1.1$ meV and $\nu_2=55.257\pm0.010$ meV. The corresponding values obtained from a study of the optical emission spectrum by Gauyacq *et al.*[18] are -0.093, -11.889 meV, and 57.052 meV, respectively. There is thus a good agreement between the values for ϵ and ν_2 whereas our value of A is much too large. In the computation, it was found that the optimized value of A is very sensitive to the accuracy in the ionization energies used.

To conclude, the present calculations were carried out to describe, in the first place, the influence of the Renner effect on the low energy vibrational structure. As discussed above, this was apparently successful since the agreement with the experimental data is generally good as regards the energies and mostly also for the intensities. Large deviations in the intensity can be seen in some cases for allowed transitions to the $(v_1 20)\ A\ ^2\Pi_u$ ionic states which shows that long range vibronic interaction involving different electronic states as well as Fermi resonances have to be taken into consideration in order to properly describe the intensity of these transitions. It is hoped that the present study will inspire further work aiming at a satisfactory description also of these effects.

ACKNOWLEDGMENTS

This work was supported by the Swedish Natural Science Research Council (NFR), the Swedish Institute and the Research Grant Council (RGC) of Hong Kong (Grant No. HKP 151/93E). During the completion of this work, one of the authors (L.K.) was employed as a research fellow at the Department of Applied Biology and Chemical Technology of The Hong Kong Polytechnic University and one of the authors (J.H.D.E.) was working as a guest scientist at the Department of Physics in Uppsala.

[1] M. I. Al-Joboury, D. P. May, and D. W. Turner, J. Chem. Soc. 6350 (1965).
[2] D. W. Turner and D. P. May, J. Chem. Phys. **46**, 1156 (1967).
[3] J. H. D. Eland and C. J. Danby, Int. J. Mass Spectrom. Ion Phys. **1**, 111 (1968).
[4] J. E. Collin and P. Natalis, Int. J. Mass Spectrom. Ion Phys. **1**, 121 (1968).
[5] C. R. Brundle and D. W. Turner, Int. J. Mass Spectrom. Ion Phys. **2**, 195 (1969).
[6] D. W. Turner, C. Baker, A. D. Baker, and C. R. Brundle, *Molecular Photoelectron Spectroscopy* (Wiley Interscience, London, 1970).
[7] A. W. Potts and G. H. Fattahallah, J. Phys. B **13**, 2545 (1980).
[8] B. Kovac, J. Chem. Phys. **78**, 1684 (1983).
[9] I. Reineck, C. Nohre, R. Maripuu, P. Lodin, S. H. Al-Shamma, H. Veenhuizen, L. Karlsson, and K. Siegbahn, Chem. Phys. **78**, 311 (1983).
[10] H. Veenhuizen, B. Wannberg, L. Mattsson, K.-E. Norell, C. Nohre, L. Karlsson, and K. Siegbahn, J. Electron Spectrosc. **41**, 205 (1986).
[11] S. Leach, M. Devoret, and J. H. D. Eland, Chem. Phys. **33**, 113 (1978).
[12] L.-S. Wang, J. E. Reutt, Y. T. Lee, and D. A. Shirley, J. Electron Spectrosc. **47**, 167 (1988).
[13] C. F. Batten, J. A. Taylor, and G. G. Meisels, J. Chem. Phys. **65**, 3316 (1976).
[14] T. Baer and P. M. Guyon, J. Chem. Phys. **85**, 4765 (1986).
[15] R. Frey, B. Gotchev, O. F. Kalman, W. B. Peatman, H. Pollak, and E. W. Schlag, Chem. Phys. **21**, 89 (1977).
[16] S. Mrozowski, Phys. Rev. **60**, 730 (1941); **62**, 270 (1942); **72**, 682 (1947).
[17] D. Gauyacq, M. Horani, S. Leach, and J. Rostas, Can. J. Phys. **53**, 2040 (1975).
[18] D. Gauyacq, C. Larcher, and J. Rostas, Can. J. Phys. **57**, 1634 (1979).
[19] C. Larcher, D. Gauyacq, and J. Rostas, J. Chim. Phys. **77**, 655 (1980).
[20] M. A. Johnson, J. Rostas, and R. N. Zare, Chem. Phys. Lett. **92**, 225 (1982).
[21] J. Rostas and R. P. Tuckett, J. Mol. Spectrosc. **96**, 77 (1982).
[22] M. A. Johnson, R. N. Zare, J. Rostas, and S. Leach, J. Chem. Phys. **80**, 2047 (1984).
[23] T. J. Sears, Mol. Phys. **59**, 259 (1986).
[24] J. M. Frye and T. J. Sears, Mol. Phys. **62**, 919 (1987).
[25] M. Larzilliere and Ch. Jungen, Mol. Phys. **67**, 807 (1989).
[26] M. Brommer, G. Chambaud, E.-A. Reinsch, P. Rosmus, A. Spielfiedel, N. Feautrier, and H.-J. Werner, J. Chem. Phys. **94**, 8070 (1991).
[27] G. Chambaud, W. Gabriel, P. Rosmus, and J. Rostas, J. Phys. Chem. **96**, 3285 (1992).
[28] F. Merkt, S. R. Mackenzie, R. J. Rednall, and T. P. Softley, J. Chem. Phys. **99**, 8430 (1993).
[29] M. A. Johnson and J. Rostas, Mol. Phys. **85**, 839 (1995).
[30] P. Baltzer, L. Karlsson, M. Lundqvist, and B. Wannberg, Rev. Sci. Instrum. **64**, 217 (1993).
[31] The ECR source is commercially available as ''VUV-5000'' from Gammadata Mätteknik AB, Box 15120, S-750 15 Uppsala, Sweden.
[32] C. E. Moore, Atomic Energy Levels, Natl. Bur. Stand. (U.S.) Circ. No. 467 (U.S. GPO, Washington, DC, 1949).
[33] E. Renner, Z. Phys. **92**, 172 (1934).
[34] J. A. Pople, Mol. Phys. **3**, 172 (1960).
[35] Ch. Jungen and A. J. Merer, *The Renner Effect, in Molecular Spectroscopy: Modern Research*, edited by K. N. Rao (Academic, New York, 1976), Vol. II.
[36] P. E. Gill, W. Murray, and M. H. Wright, *Practical Optimization* (Academic, London, 1981).
[37] S. Bell and P. A. Warsop, J. Mol. Spectrosc. **20**, 425 (1966).
[38] P. Baltzer, B. Wannberg, M. Lundqvist, L. Karlsson, D. M. P. Holland, M. A. MacDonald, M. A. Hayes, and W. von Niessen, Chem. Phys. in print.